Optimal Divergent and Elliptical Angle of Gaussian Beams in Trap Relying on Optical Pumping

Chanyeong Seo

Trapped Ion Quantum Information Group, ETH Zürich, Otto-Stern-Weg 1, 8093 Zürich, Switzerland
Georgia Institute of Technology, 225 North Avenue NW, Atlanta, Georgia 30332, USA

cseo33@gatech.edu

Abstract. Cooling and trapping neutral atoms is essential for quantum technologies and precision measurement. To cool atoms, lasers can be used to exert forces that slow the motion of the atoms, as if they move inside a dense fluid. Inside a magneto-optical trap (MOT), atoms can be conveniently cooled down to 1 mK by superimposing six laser beams in combination with a magnetic field gradient. Recently, a MOT has been realized by delivering divergent light directly from optical fibers to atoms, providing a compact, miniaturizable configuration. It has been shown that this system can further be simplified by removing the magnetic field gradient in a so-called trap relying on optical pumping (TROOP), which achieves confinement using only divergent laser light. To extend the fiber approach to TROOP effectively, we investigate the influence of divergence and polarization angles on trapping behavior and identify the optimal angles. We perform Monte Carlo trajectory simulations of cesium atoms on the $J_g = 4 \rightarrow J_e = 5$ transition to identify optimal divergent and elliptical angles at fixed initial beam power $I_{\text{initial}} = 1.11 \times 10^9$ W/m^2 and find that a beam divergence near 8° and perfectly circular polarization maximize trapping stability, whereas for angles smaller than 5°, the system reflects the behavior of an optical molasses with vanishing confinement.

INTRODUCTION

Trapping and cooling neutral atoms to ultracold temperatures, near absolute zero, has offered advances in quantum technology and precision measurement for cutting-edge applications, such as ultraprecise atomic clocks and qubits in emerging quantum computers. Cooling atoms refers to reducing their speed because the temperature is proportional to the average kinetic energy of the atoms. This can be achieved by illuminating the atoms with laser beams whose frequency is below an atomic resonance, called red-detuned beams, which exert a process known as Doppler cooling.

Consider a two-level atom with ground state E_g, excited state E_e, and resonance frequency ω_0 interacting with two counterpropagating laser beams of frequency ω, red-detuned by $\delta_0 < 0$, as illustrated in Fig. 1(a). For a stationary atom, both beams are equally likely to be absorbed because absorption is more probable when the beam frequency seen by the atom ω_{eff} is closer to the atomic resonance ω_0 and the beams have the same frequency ω. However, if the atom has a velocity, the Doppler effect shifts the beam frequencies in the perspective of the atom. As shown in Fig. 1(b), an atom moving to the right perceives a higher effective frequency $\omega_{\text{eff,right}}$ from the left-going beam and a lower effective frequency $\omega_{\text{eff,left}}$ from the opposite beam. Since absorption is more probable when the effective frequency is closer to the atomic resonance ω_0, the photons are preferentially absorbed from the beam opposing the atomic motion as $\omega_{\text{eff,right}} \approx \omega_0$ and $\delta_{\text{eff,right}} \approx 0$. Each absorption event transfers photon momentum, which in the red-detuned case, together with the Doppler shift, produces a velocity-dependent force that reduces the speed of the atom, called a Doppler cooling process.

To dampen the velocity of atoms in all directions, an optical molasses (OM) is yielded by arranging six counterpropagating beams along the x, y and z axes. As if the atoms move inside dense honey, they are slowed and cooled down to their theoretical lowest temperature, the Doppler temperature, typically on the order of hundreds of microkelvins. At this temperature, the motion of the atoms is too slow to produce a significant enough Doppler shift. Once the atoms are at the near-stationary state, they lose preferential absorbance of photons as in Fig. 1(a) with $\omega_{\text{eff,left}} \approx \omega_{\text{eff,right}}$, absorb a photon in any direction, and scatter in a random direction by reemitting the photon. Thus, although the OM cools and thus slows down the atoms, they eventually diffuse out of the interaction region with the laser beams and are lost. To overcome this lack of positional confinement in OM, a MOT combines Doppler cooling and magnetic fields. A magnetic field changes the atomic resonance transition similar to the Doppler effect. A position-dependent magnetic field combined with the OM laser beam configuration provides both the Doppler cooling and the restoring force toward the trap center simultaneously, ensuring that the cold atom remains at the center with a true confinement of ultracold atoms. In this work, we explore a different approach that provides a position-dependent restoring force without the need for a magnetic field, a trap relying on optical pumping (TROOP) [1]. The TROOP completely replaces the role of the magnetic fields with an optical pumping process using six divergent polarized beams to achieve

confinement, shown in Fig. 1(c). Carefully chosen polarizations among σ^+, π, and σ^- pump the electron into a specific energy level, shown in Fig. 1(d), which absorbs more photons from the lasers that offer position-dependent force; this process is named optical pumping. The optical pumping process will be explored thoroughly in the section on the TROOP Trapping Mechanism.

To create divergent beams in conventional free space, macroscopic lenses and six beams should be carefully aligned, which is experimentally demanding and sensitive to misalignment. Recently, a compact MOT design has been demonstrated by achieving divergent light directly from optical fibers to atoms [2]. This fiber-based approach fixes the beam geometry by construction, reducing the optical alignment complexity and providing a compact, miniaturizable configuration. To extend this approach to TROOP, which inherently requires divergent beams, we theoretically investigated how their divergence and polarization angles influence the resulting trapping behavior and identify optimal angles. We modeled the three-dimensional motion of cesium atoms in optical pumping between the energy level transition $J_g = 4 \rightarrow J_e = 5$ using a Monte Carlo trajectory simulation. Throughout the simulation, the beams have the power $I_{\text{initial}} = 1.11 \times 10^9$ W/m^2 to set a Rabi frequency Ω at the center similar to the natural decay rate of cesium Γ, following the choice of these parameters from the previous investigation [1]. Here, Ω measures how strongly the laser drives transitions between ground and excited states, while Γ describes how quickly electrons return to ground states from excited states. Operating with $\Omega \approx \Gamma$ keeps electrons in ground states, so they can continue to preferentially absorb photons from the beams. We expect that this theoretical exploration introduces and optimizes the optical fiber-based TROOP experiment, facilitating integration into compact quantum device-scale platforms.

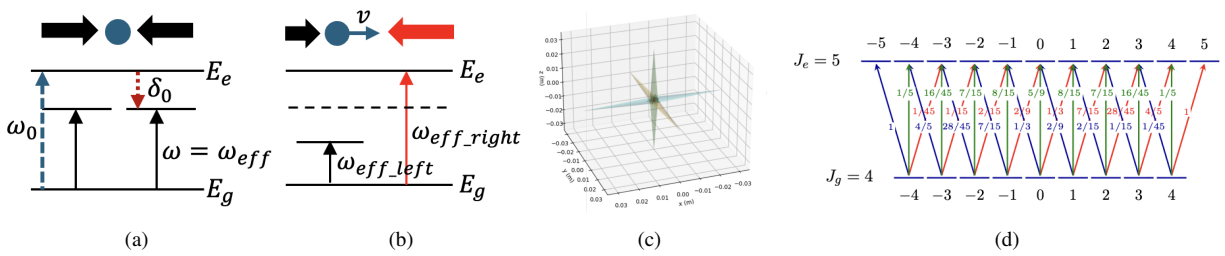

FIGURE 1. (a) Energy diagram for a stationary two-level atom with ground state E_g and excited state E_e. An atom (blue circle) is shown between two counterpropagating laser beams, whose arrow lengths are drawn proportional to the frequencies seen in the perspective of the atom. The atom has a resonance frequency ω_0, while the laser beams have frequency ω that is red-detuned from resonance by $\delta_0 = \omega - \omega_0 < 0$. (b) When the atom moves to the right with velocity $\mathbf{v}$, the Doppler effect shifts the frequencies of the two beams in the atomic frame. For an atom moving to the right, the left-going beam is shifted closer to resonance $\omega_{\text{eff,right}}$ (red arrows) and a decreased effective frequency $\omega_{\text{eff,left}}$. The atom then preferentially absorbs photons from the left-going beam. (c) Example TROOP geometry with six divergent beam. (d) Energy transitions $J_g = 4 \rightarrow J_e = 5$ with $\sigma^{\pm}$ and π couplings labeled by the squared Clebsch–Gordan (CG) coefficients. J_g has 9 ground states from $m_g = -4$ to $m_g = 4$ and J_e has 11 excited states from $m_e = -5$ to $m_e = 5$. The red, green, and blue lines and numbers show the electron's movement for the polarization components σ^+, π, and σ^-, respectively, and the corresponding $(C_q(m_g \rightarrow m_e))^2$ for each $m_g \rightarrow m_e$ transition pair.

THEORY

TROOP Trapping Mechanism

In addition to the Doppler effect, the traditional TROOP setup uses six divergent Gaussian laser beams, red-detuned from atomic resonance, arranged along the x, y, and z axes, as shown in Fig. 1(c). All beams are circularly polarized, but significantly, their helicities are arranged in a mixed configuration which must satisfy condition $h_z = -h_x = -h_y$ [1]. Off-center, the atom feels an intensity imbalance in the three possible polarization components of light (σ^+, π, σ^-), and this imbalance contributes a net restorative force. Furthermore, nonuniform transition probabilities associated with the various polarizations amplify biased preference in the polarity of the light. This is governed by the squared Clebsch–Gordan (CG) coefficient for an atom's ground-state magnetic quantum number m_g to an excited-state magnetic quantum number m_e pair, shown in Fig. 1(d). The magnitude of the squared Clebsch–Gordan coefficient $C_q^2(m_g \rightarrow m_e)$ reflects the probability of the polarization q to excite the atom from m_g.

For example, suppose that $h_z = -1$ and a cesium atom is in $z > 0$ and $m_g = 0$. Since the Clebsch–Gordan coefficients

for all polarizations are equal to $1/3$ as shown in Fig. 1(d), σ^- polarized light, the highest intensity, is likely to be absorbed. Once an atom begins to absorb preferentially, optical pumping drives its internal state to reinforce that bias. From $m_g = 0$, the absorption of a σ^- photon excites to $m_e = -1$, with spontaneous decay likely to $m_g = -1$. From there, σ^- absorption is favored over σ^+ because $C_q^2(-1 \to -2) = 7/15$ exceeds $C_q^2(-1 \to 0) = 2/15$. Repeated cycles pump the atom to $m_g = -4$, where the σ^- transition to $m_e = -5$ is strongly preferred, suppressing the σ^+ transition from $m_g = -4$ to $m_e = -3$ by a factor of 45. Thus, both the intensity imbalance in the polarizations and the optical pumping contribute to the biased photon absorption of σ^- that forces the atom to $-\hat{z}$ from $z > 0$, toward the center. After crossing the origin ($z < 0$) the atom remains in $m_g = -4$ and continues to absorb σ^-, so the force still points towards $-\hat{z}$. Reversing the direction of the force requires pumping to $m_g = +4$ so that σ^+ dominates. Direct σ^+ excitation from $m_g = -4 \to m_e = -3$ is still strongly suppressed, and awaiting a large intensity imbalance leads to deviation from the trapping radius of the experiment. Instead, a π component offers an alternative path by exciting the electron from $m_g = -4$ to $m_e = -4$, followed by spontaneous decay to $m_g = -3$ preferentially, eventually reaching $m_g = +4$ and restoring a force towards $+\hat{z}$. The formation of π-polarized light is shown in Appendix A, and the force fields for different m_g states, divergent angles, and elliptical angles are presented in Appendices B, C, and D, respectively.

Monte Carlo Simulation Algorithm

When a ground-state sublevel m_g absorbs a photon, the excited magnetic quantum number is $m_e = m_g + 1$ for σ^+, $m_e = m_g$ for π, and $m_e = m_g - 1$ for σ^-, as shown in Fig. 1(d). For each beam j, we calculate the corresponding scattering rate using the effective detuning of the beam, including the Doppler shift and the local intensity of each spherical component shown in Eqs. (16a)–(16d). The scattering rate for that channel is proportional to the squared Rabi frequency Ω_{jq}^2 and the squared CG coefficient $C_q^2(m_g \to m_e)$ [3]. Summing over all beams and polarizations gives the total scattering rate R_{tot} [4]. For a small time step Δt, a scattering event is accepted with probability $P = R_{\text{tot}}\Delta t \ll 1$ [5]. If it scatters, we choose the specific beam and and update the atomic velocity according to the photon momentum. If no scattering occurs, the atom propagates ballistically. The detailed Monte Carlo simulation algorithm is explained in Appendix E. For this study, the initial beam intensity was fixed at $I_{\text{initial}} = 1.11 \times 10^9\,\text{W/m}^2$, and all six beams were positioned 3.5 cm from the origin, directed toward the center. We used a natural linewidth of $\Gamma = 2\pi \times 5.2$ MHz and a red-detuning of $\delta_0 = -\Gamma$ for all beams, with helicities satisfying $h_z = -h_x = -h_y = 1$.

RESULTS AND DISCUSSION

Optimal Divergent Angle of Beams

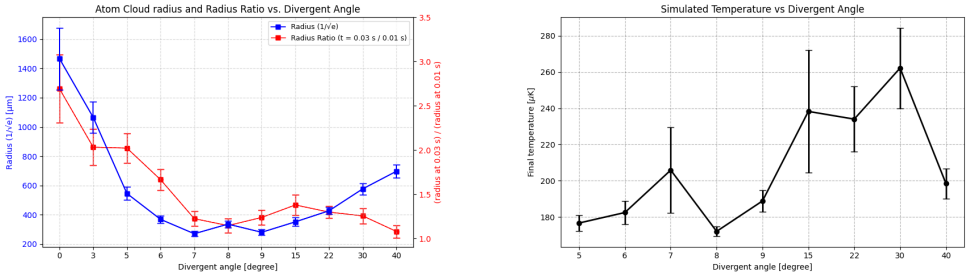

(a) (b)

FIGURE 2. Data is for a fixed peak intensity $I_{\text{initial}} = 1.11 \times 10^9\,\text{W/m}^2$ and elliptical angle 45°. (a) The blue curve shows variation of the largest $1/\sqrt{e}$ radius of the atomic cloud with beam divergence angle, and the red curve shows the ratio of the largest radius at $t = 0.03$ s to that at $t = 0.01$ s. (b) Simulated mean atomic temperature vs beam divergence angle. The error bars indicate standard error (SE) of the mean; radius SEs are computed across trajectories, and ratio SEs use first-order error propagation.

The blue curve in Fig. 2(a) shows that the trapping radius reaches the minimum level at 7° and 9°. Lower and higher

angles lead to higher trapping radii. To assess trapping stability independent of absolute size, the red curve shows how the trapping radius dispersed over time. For divergent angles less than 5°, this ratio exceeds 2.0, and the cloud remains relatively large despite temperatures near the Doppler limit, indicating a crossover to optical molasses. For angles larger than 15°, the radius increases even as the ratio approaches unity, consistent with a reduced intensity on the axis at large divergence and therefore weaker scattering and trapping. Figure. 2(b) shows that the mean temperature exhibits a minimum near 8° and then rises as the divergence increases, reflecting the decreased cooling efficiency.

Optimal Elliptical Angle of Beams

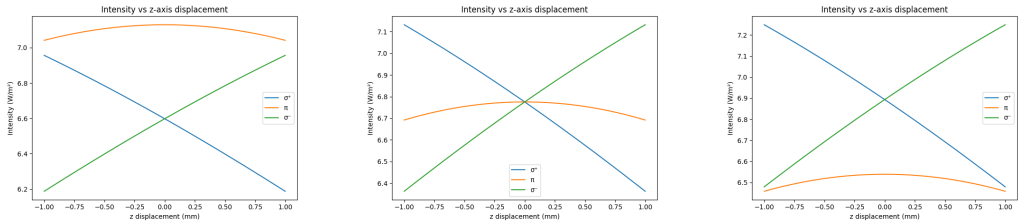

(a) (b) (c)

FIGURE 3. Intensity distributions of σ^+ (blue), π (orange), and σ^- (green) along the z quantization axis with an elliptical angle of (a) 44.5°, (b) 45° (perfect circular polarization), and (c) 45.5° when all six beams were divergent by 22°.

The simulations indicate that TROOP performance is highly sensitive to polarization ellipticity. We identified an optimal value of 45°, perfect circular polarization, and the small deviation of the elliptical angle causes diffusion within 0.01 s. As shown in Fig. (3), deviations from 45° increase or decrease the π component along the quantization axis, breaking the intensity symmetry between π and $\sigma^{\pm}$ and suppressing the required biased absorption. Consequently, the trap becomes almost identical to optical molasses, losing confinement.

CONCLUSION

We have performed Monte Carlo trajectory simulations to investigate the optimal beam configuration for a TROOP. The results demonstrate that a divergent angle near 8° yields the most favorable balance between the trapping radius, stability, and temperature, optimizing the system. Smaller angles than 5° lead to optical molasses, while larger angles reduce the efficiency of scattering. Likewise, the simulations confirm that TROOP is highly sensitive to polarization circularity, with the optimal elliptical angle of 45° corresponding to perfect circular polarization. Any deviation from this condition enhances the π component and suppresses the necessary imbalance between the σ^+ and σ^- transitions, thus weakening the trap. These findings establish the optical fiber-based design criteria for optimizing the performance of TROOP, guiding the development of simpler and more portable configurations for future quantum technologies. We suggest investigating the effect of initial beam intensities on TROOP in the future work.

ACKNOWLEDGMENTS

We thank Dr. Henrik Hirzler and Dr. Jonathan Home for their supervision and this invaluable opportunity.

REFERENCES

1. P. Bouyer, P. Lemonde, M. Ben Dahan, A. Michaud, C. Salomon, and J. Dalibard, Europhys. Lett. **27**, 569–574 (1994).
2. C. S. Nichols, L. M. Nofs, M. A. Viray, L. Ma, E. Paradis, and G. Raithel, Phys. Rev. Appl. **14**, 044013 (2020).
3. R. D. Glover, J. E. Calvert, and R. T. Sang, Phys. Rev. A **87**, 023415 (2013).
4. F. Atoneche and A. Kastberg, Eur. J. Phys. **38**, 045703 (2017).
5. R. K. Hanley, P. Huillery, N. C. Keegan, A. D. Bounds, D. Boddy, R. Faoro, and M. P. A. Jones, J. Mod. Opt. **65**, 667–676 (2018).

APPENDIX

Appendix A: Electric Field and Intensity Calculation by Polarization Decomposition

In this section, we calculate the electric field and intensity felt by an atom for each helicity at position $\mathbf{r}$ by coherently summing six focused Gaussian beams.

A.1 TROOP beam geometry and Gaussian field

This simulation employs six divergent Gaussian beams, with details in the Monte Carlo Simulation Algorithm section. Each beam $j = 1,\ldots,6$ is a Gaussian mode focused at $\mathbf{r}_{\text{focus,j}}$ and propagating along nominal axis $\hat{k}_j$. At any point $\mathbf{r}$ we define

$$\mathbf{R}_j = \mathbf{r} - \mathbf{r}_{\text{focus,j}}, \tag{1a}$$

$$z_j = \hat{k}_j \cdot \mathbf{R}_j, \tag{1b}$$

$$\mathbf{R}_{\perp,j} = \mathbf{R}_j - z_j \hat{k}_j, \tag{1c}$$

$$\rho_j = \|\mathbf{R}_{\perp,j}\|. \tag{1d}$$

The local beam radius, wavefront curvature, and Gouy phase are

$$w(z_j) = w_0 \sqrt{1 + (z_j/z_R)^2}, \tag{2a}$$

$$R(z_j) = z_j \Big(1 + (z_R/z_j)^2\Big), \tag{2b}$$

$$\phi_G = \arctan\big(z_j/z_R\big). \tag{2c}$$

The complex scalar envelope is

$$A_j(\mathbf{r}) = \frac{w_0}{w(z_j)} \exp\Big[-\tfrac{\rho_j^2}{w(z_j)^2}\Big] \exp\Big[i\big(k_0 z_j + \tfrac{k_0 \rho_j^2}{2R(z_j)} - \phi_G\big)\Big], \tag{3}$$

with $k_0 = 2\pi/\lambda$, and is normalized so that at focus $|\mathbf{E}_j| = E_0$.

A.2 Local propagation direction and transverse basis

Because of the curved wavefront, the true local wavevector deviates from $\hat{k}_j$. We define

$$\mathbf{k}_{\text{loc},j} = \hat{k}_j + \frac{\mathbf{R}_{\perp,j}}{R(z_j)}, \tag{4a}$$

$$\hat{k}_{\text{loc},j} = \frac{\mathbf{k}_{\text{loc},j}}{\|\mathbf{k}_{\text{loc},j}\|}. \tag{4b}$$

To span the transverse plane orthogonal to $\hat{k}_{\text{loc},j}$ we pick a reference axis $\hat{r}_j$ for the Cartesian direction least aligned with $\hat{k}_{\text{loc},j}$, then set

$$\mathbf{e}_{1,j} = \frac{\hat{k}_{\text{loc},j} \times \hat{r}_j}{\big\|\hat{k}_{\text{loc},j} \times \hat{r}_j\big\|}, \tag{5a}$$

$$\mathbf{e}_{2,j} = \frac{\hat{k}_{\text{loc},j} \times \mathbf{e}_{1,j}}{\big\|\hat{k}_{\text{loc},j} \times \mathbf{e}_{1,j}\big\|}. \tag{5b}$$

A.3 Jones-vector description of polarization

In this local basis $\{\mathbf{e}_{1,j}, \mathbf{e}_{2,j}\}$ any purely transverse polarization can be written as a Jones vector as follows:

$$\mathbf{p}_j = \begin{pmatrix} p_{1,j} \\ p_{2,j} \end{pmatrix} \quad \longleftrightarrow \quad p_{1,j}\,\mathbf{e}_{1,j} \,+\, p_{2,j}\,\mathbf{e}_{2,j}\,. \tag{6a}$$

For an elliptically polarized beam of helicity $h_j = \pm 1$ and ellipticity angle α ($\alpha = \pi/4$ indicates circular polarization), the components are

$$\begin{pmatrix} p_{1,j} \\ p_{2,j} \end{pmatrix} = \begin{pmatrix} \cos\alpha \\ i\,h_j \sin\alpha \end{pmatrix}. \tag{6b}$$

Thus, each beam's total complex electric field is

$$\mathbf{E}_j(\mathbf{r}) = E_0 A_j(\mathbf{r}) \left[p_{1,j}\,\mathbf{e}_{1,j} + p_{2,j}\,\mathbf{e}_{2,j} \right] \;\longleftrightarrow\; E_0 A_j(\mathbf{r}) \begin{pmatrix} p_{1,j} \\ p_{2,j} \end{pmatrix}_j . \tag{6c}$$

A.4 Decomposition into spherical components

Finally, the atom's quantization axis $\hat{q}$ is chosen dynamically because an external magnetic field is absent. We now describe in detail how the local electric field felt by an atom at position $\mathbf{r}$ is constructed as the coherent superposition of six divergent, elliptically polarized Gaussian beams, decomposed into the spherical polarization components relative to a quantization axis, and how the resulting intensities feed into optical pumping and scattering rates. We build an orthonormal frame

$$\mathbf{e}_{\perp 1} = \frac{\hat{q} \times \hat{r}_q}{\|\hat{q} \times \hat{r}_q\|}, \tag{7a}$$

$$\mathbf{e}_{\perp 2} = \frac{\hat{q} \times \mathbf{e}_{\perp 1}}{\|\hat{q} \times \mathbf{e}_{\perp 1}\|}, \tag{7b}$$

with $\hat{r}_q$ the least-aligned Cartesian axis. we project each beam as follows:

$$E_{1,j} = \mathbf{E}_j \cdot \mathbf{e}_{\perp 1}, \tag{8a}$$

$$E_{2,j} = \mathbf{E}_j \cdot \mathbf{e}_{\perp 2}, \tag{8b}$$

$$E_{\parallel,j} = \mathbf{E}_j \cdot \hat{q}. \tag{8c}$$

We then define the spherical components in the standard way,

$$E_{\sigma^+,j} = \tfrac{E_{1,j} - i E_{2,j}}{\sqrt{2}}, \tag{9a}$$

$$E_{\pi,j} = E_{\parallel,j}, \tag{9b}$$

$$E_{\sigma^-,j} = \tfrac{E_{1,j} + i E_{2,j}}{\sqrt{2}}. \tag{9c}$$

Collecting these into a 3×6 coupling matrix W (rows σ^+, π, σ^-, column j) gives the intensities $|E_{q,j}|^2$ that drive optical pumping and scattering in our Monte Carlo simulation.

We collect these into a coupling matrix $\mathbf{W}$ of size 3×6 where row indices are $(\sigma^+, \pi, \sigma^-)$ and column j corresponds to beam j,

$$W_{qj} = \begin{bmatrix} E_{\sigma^+,1} & \cdots & E_{\sigma^+,6} \\ E_{\pi,1} & \cdots & E_{\pi,6} \\ E_{\sigma^-,1} & \cdots & E_{\sigma^-,6} \end{bmatrix}. \tag{10}$$

A.5 Intensity distribution of each polarization

Using the derived coupling matrix W, the intensity associated with each spherical component of each beam is

$$I_{qj} = \frac{1}{2} c\varepsilon_0 |W_{qj}|^2, \quad q \in \{\sigma^+, \pi, \sigma^-\}. \tag{11a}$$

The total intensity in each polarization channel is obtained by summing over beams

$$I_{\sigma^+} = \sum_j I_{\sigma^+,j}, \tag{12a}$$

$$I_{\pi} = \sum_j I_{\pi,j}, \tag{12b}$$

$$I_{\sigma^-} = \sum_j I_{\sigma^-,j}. \tag{12c}$$

For our simulation setting, the total intensity from all beams at the center for each polarization is $\sigma^+ = 6.775$, $\pi = 6.775$, and $\sigma^- = 6.775$ with the z-quantization axis shown in Fig. 4, whose values aligns with Fig. 3. The calculated field and intensity yield the distribution shown in Fig. 5. Figure. 6 illustrates the linear dependence of the

$$\mathbf{I}\,[\mathrm{W\,m^{-2}}] = \begin{array}{c} \\ \sigma^+ \\ \pi \\ \sigma^- \end{array} \begin{array}{c} \begin{array}{cccccc} \text{Beam } +x & \text{Beam } -x & \text{Beam } +y & \text{Beam } -y & \text{Beam } +z & \text{Beam } -z \end{array} \\ \begin{bmatrix} 0.846913 & 0.846913 & 0.846913 & 0.846913 & 0 & 3.38765 \\ 1.69382 & 1.69382 & 1.69382 & 1.69382 & 0 & 0 \\ 0.846913 & 0.846913 & 0.846913 & 0.846913 & 3.38765 & 0 \end{bmatrix} \end{array}$$

FIGURE 4. Intensity matrix of the Monte Carlo simulation at the origin with the six counterpropagating beams of $I_{\text{initial}} = 1.11 \times 10^9$ W/m^2 and the divergent angle of 22° from 3.5 cm away from the origin, along the z-quantization axis.

$\sigma^{\pm}$ intensities on the atomic displacement as described in Eqs. (16a)–(16d), visualizing factor 2 in the dependence on z, which is absent for the transverse coordinate ξ. Figure. 6(c) quantized along the z axis has twice higher gradients than Fig. 6(a) and 6(b) quantized along the x and y axis, respectively.

A.6 Construction of π-polarized photon

When only the two counterpropagating z beams of opposite helicity are on, with the quantization axis along z, no π intensity is produced, as shown in Fig. 7. A π–polarized component arises only on the axes orthogonal to the quantization axis. In the z-beam case, the fields are $\sigma^{\pm}$ with $\vec{E}$ confined to the XY plane, so the projection onto $+\hat{z}$ is zero. By contrast, beams along the x and y axes contribute substantially, since a circularly polarized beam on the x axis produces an $\vec{E}$ that oscillates linearly in the YZ plane. The atom perceives as π light when $\vec{E} \perp +\hat{z}$. As shown in Fig. 8, the x-axis beams contain all three components, σ^+, π, and σ^-, with an intensity of π along $+\hat{z}$ approximately twice that of the circular components. This is consistent with Stokes analysis, particularly the S_1/S_0 map in Fig. 9. By the same reasoning, only pure circular components appear along the quantization axis, as shown in Fig. 7. Therefore, the significant amount of π-polarized light on the quantization axis $+\hat{z}$ facilitates the movement of electrons between $m_g = -4$ and $m_g = +4$, creating trapping.

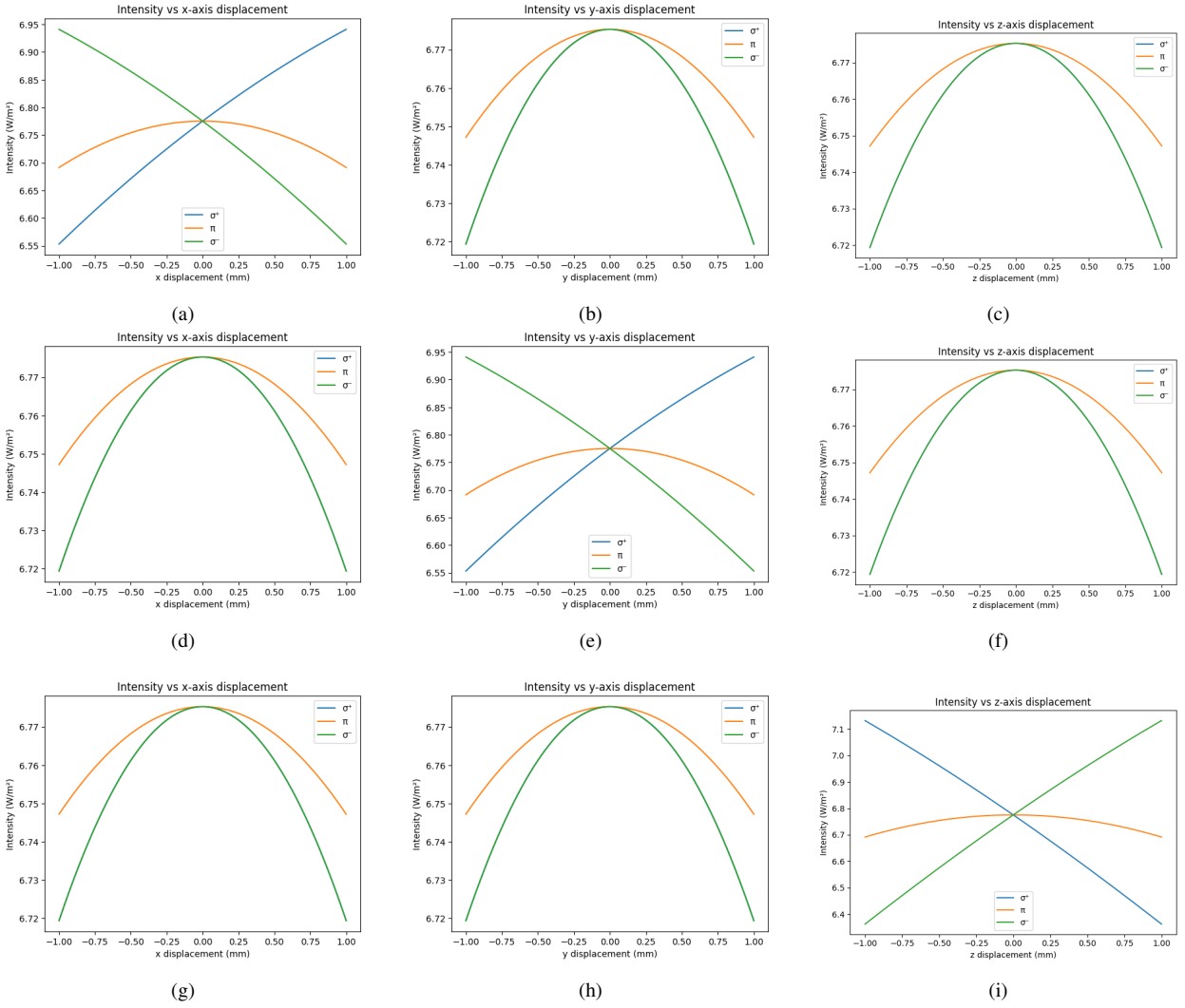

FIGURE 5. Intensity distribution of σ^+, π, and σ^- along the x, y, and z axes under three configurations. Each row represents a different quantization or elliptical setup, and each column corresponds to one spatial axis. The blue, yellow, and green curves denote σ^+, π, and σ^- polarizations, respectively.

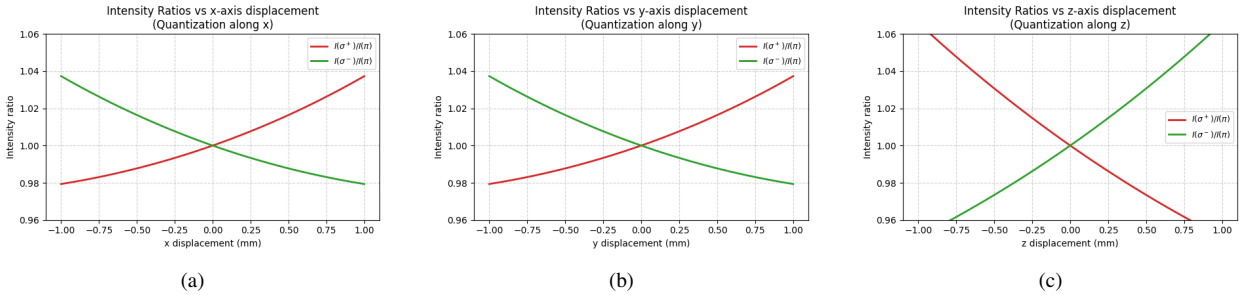

FIGURE 6. Ratios $I(\sigma^+)/I(\pi)$ (red) and $I(\sigma^-)/I(\pi)$ (green) along (a) the x axis, (b) the y axis, and (c) the z axis, with the quantization axis aligned to the plotted axis in each panel.

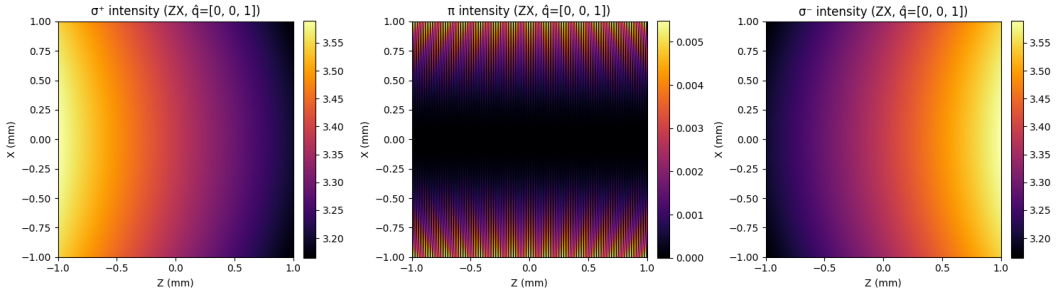

FIGURE 7. Intensity distribution of σ^+, π, and σ^- on the ZX plane when only the two z-axis beams are on, with the quantization axis along $+\hat{z}$.

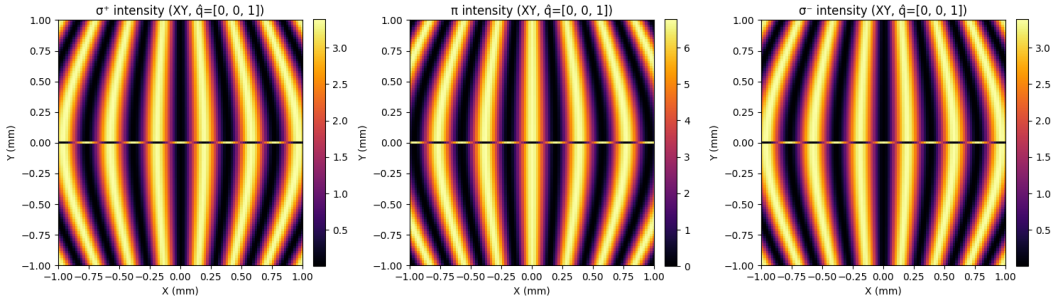

FIGURE 8. Intensity distribution of σ^+, π, and σ^- when only two beams on the x axis are turned on along a quantization axis $+\hat{z}$, without the interference with beams at other axes.

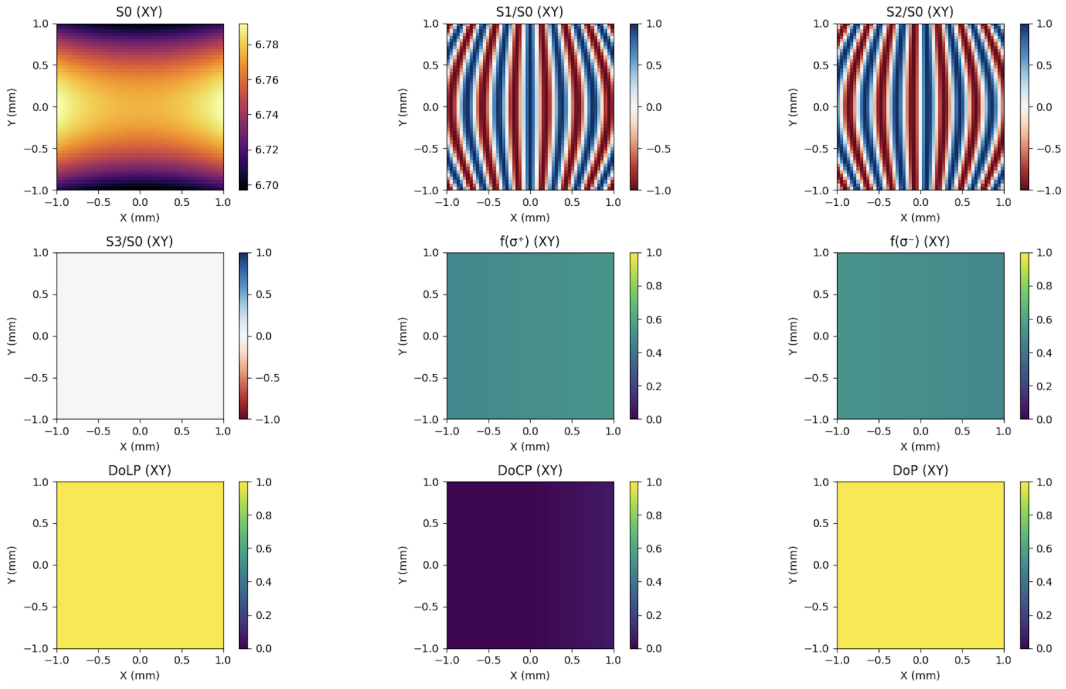

FIGURE 9. Stoke parameter on XY plane when only two beams on x axis are turned on along the quantization axis $+\hat{z}$. $S0$ is total intensity, $\frac{S_1}{S_0}$ is the ratio of linear polarized light in 90°, $\frac{S_2}{S_0}$ is the ratio of linearly polarized light in 45°, $\frac{S_3}{S_0}$ is the ratio of circularly polarized light, $f(\sigma^+)$ and $f(\sigma^-)$ is the ratio of σ^+ and σ^- lights, degree of linear polarization (DoLP) is the ratio of total linearly polarized light, degree of circular polarization (DoCP) is ratio of total circularly polarized light, degree of polarization (DoP) is the ratio of total polarized light.

Appendix B: Force Field for Each Ground State

Shown below are the simulated force fields for each ground state, calculated under the conditions described in the Monte Carlo Simulation Algorithm section, with a beam divergence of 22° and ellipticity of 45°.

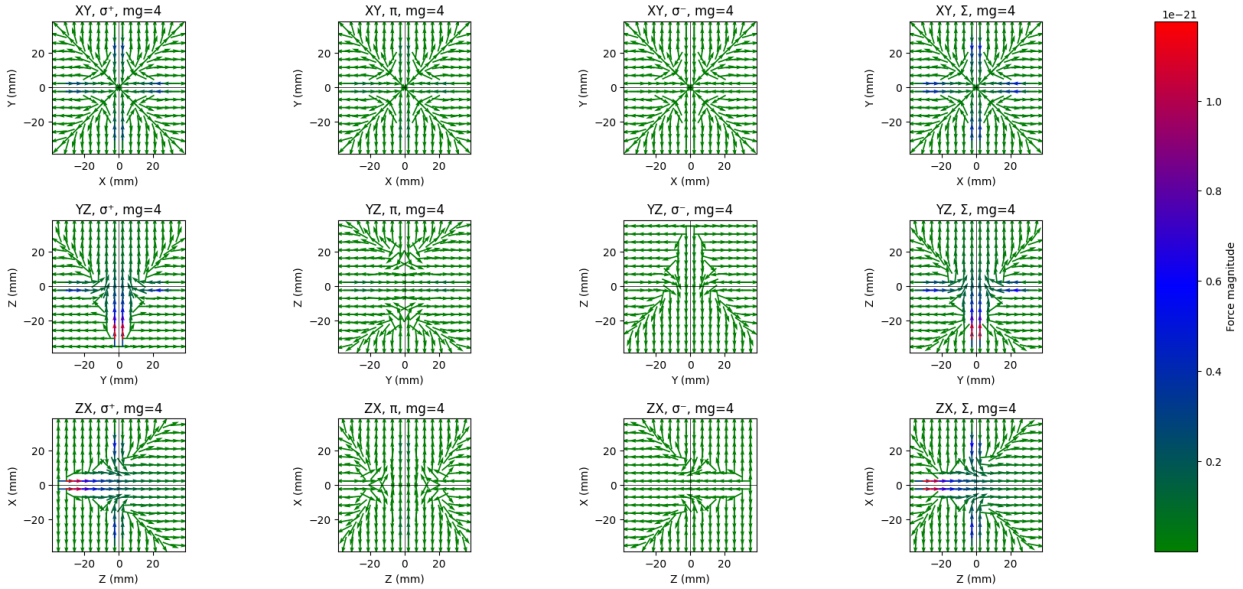

FIGURE 10. Force field when $m_g = 4$ for a stationary atom.

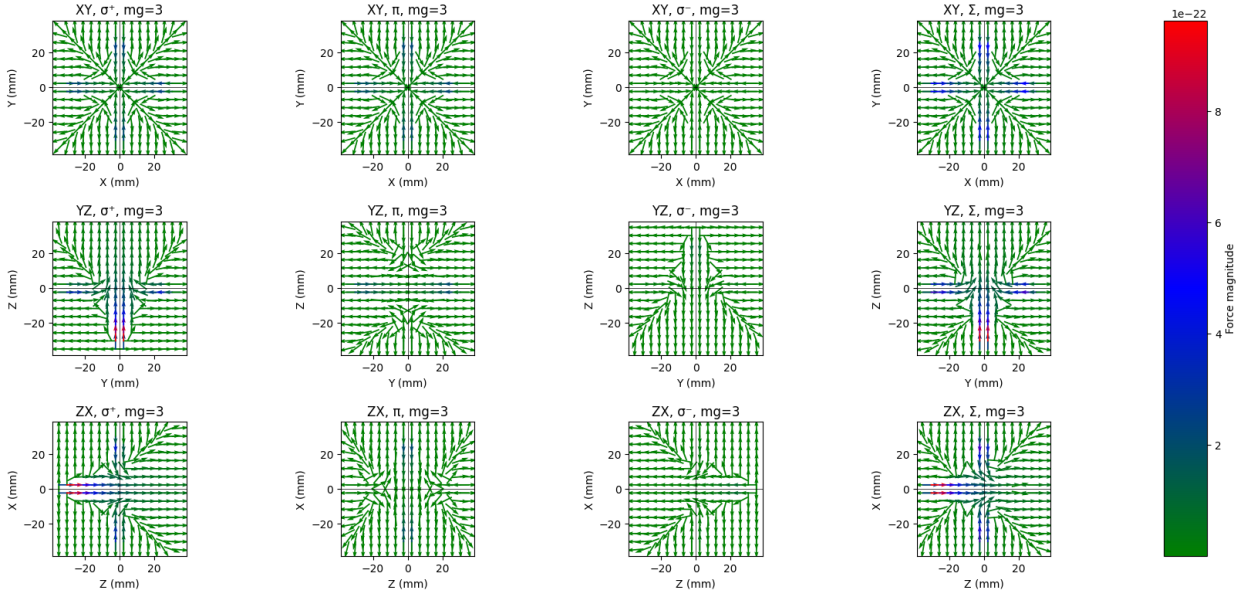

FIGURE 11. Force field when $m_g = 3$ for a stationary atom.

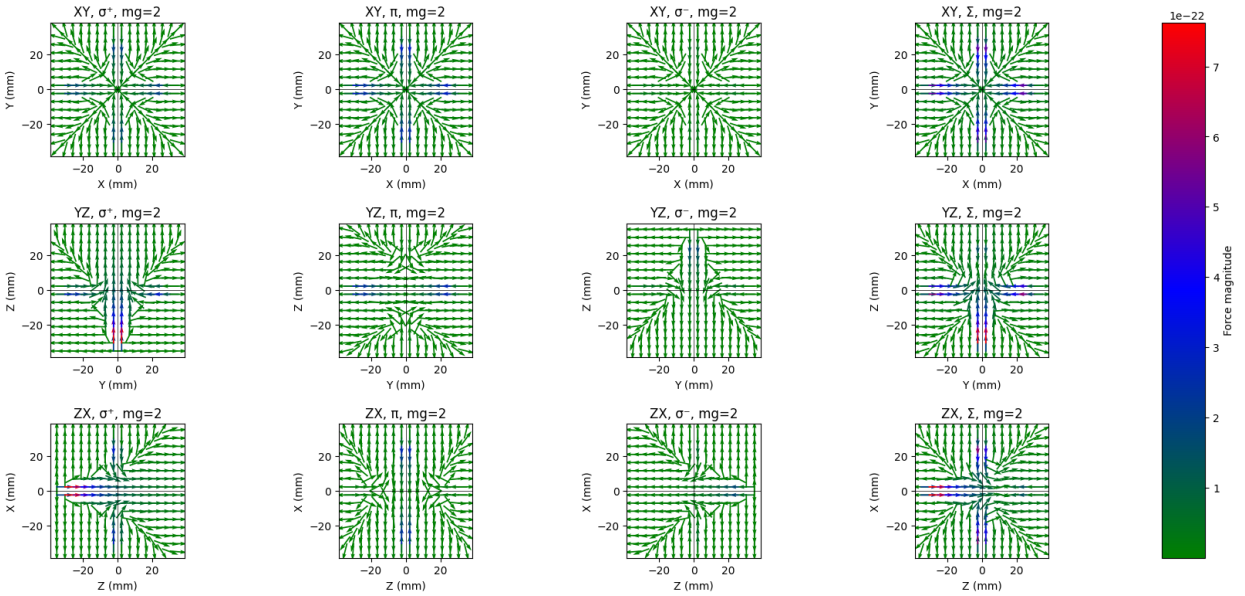

FIGURE 12. Force field when $m_g = 2$ for a stationary atom.

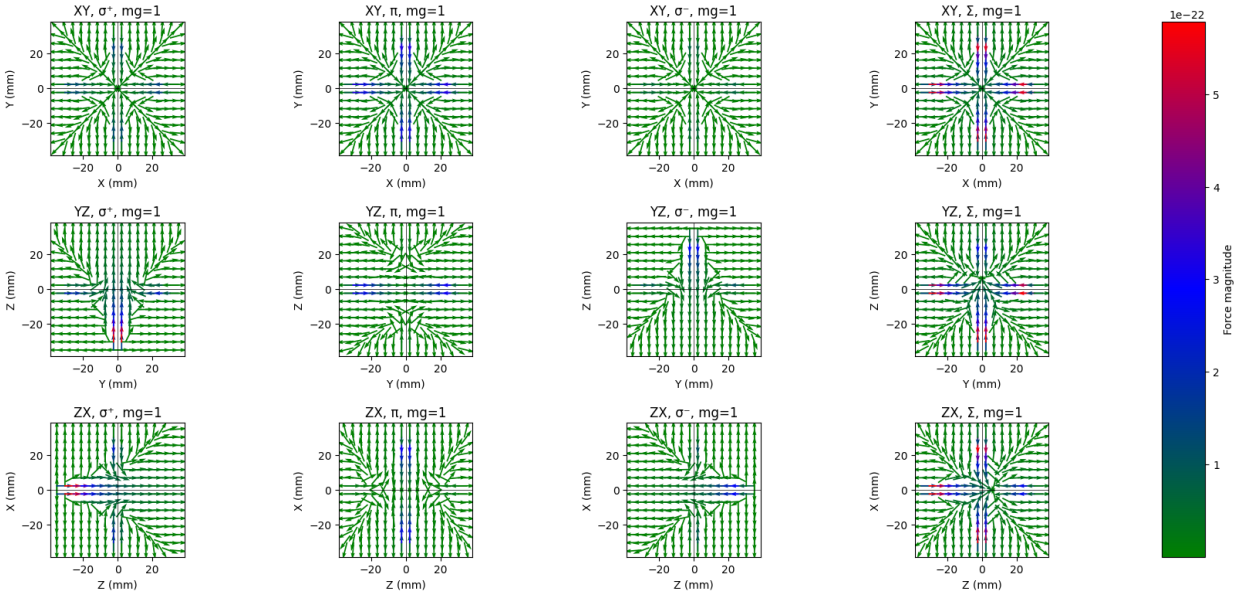

FIGURE 13. Force field when $m_g = 1$ for a stationary atom.

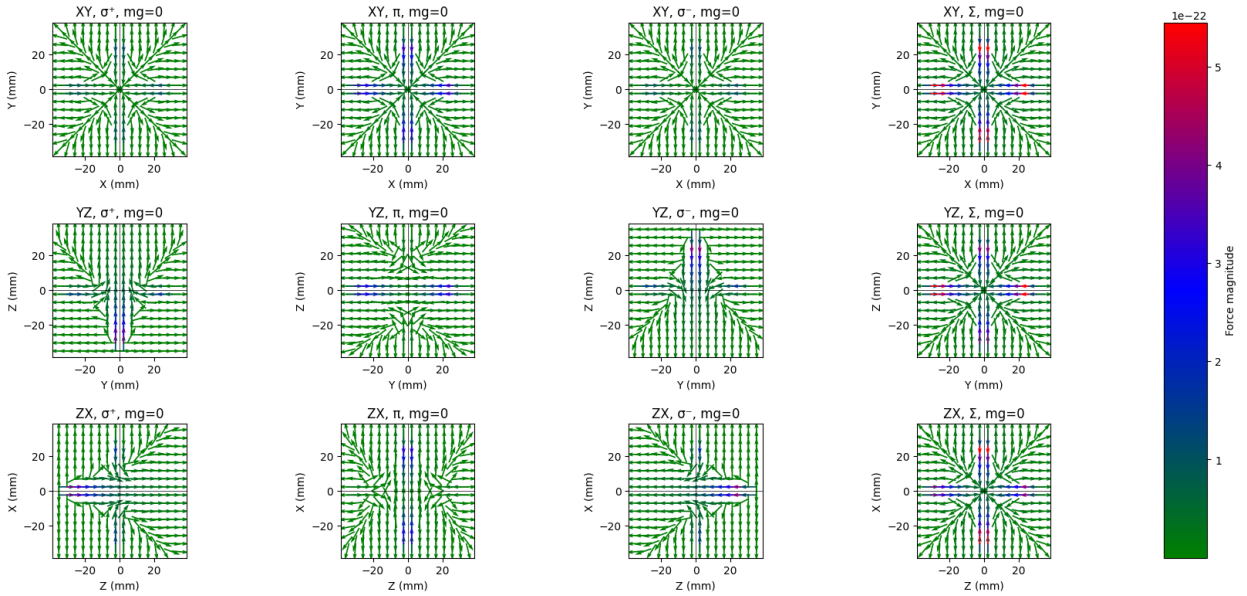

FIGURE 14. Force field when $m_g = 0$ for a stationary atom.

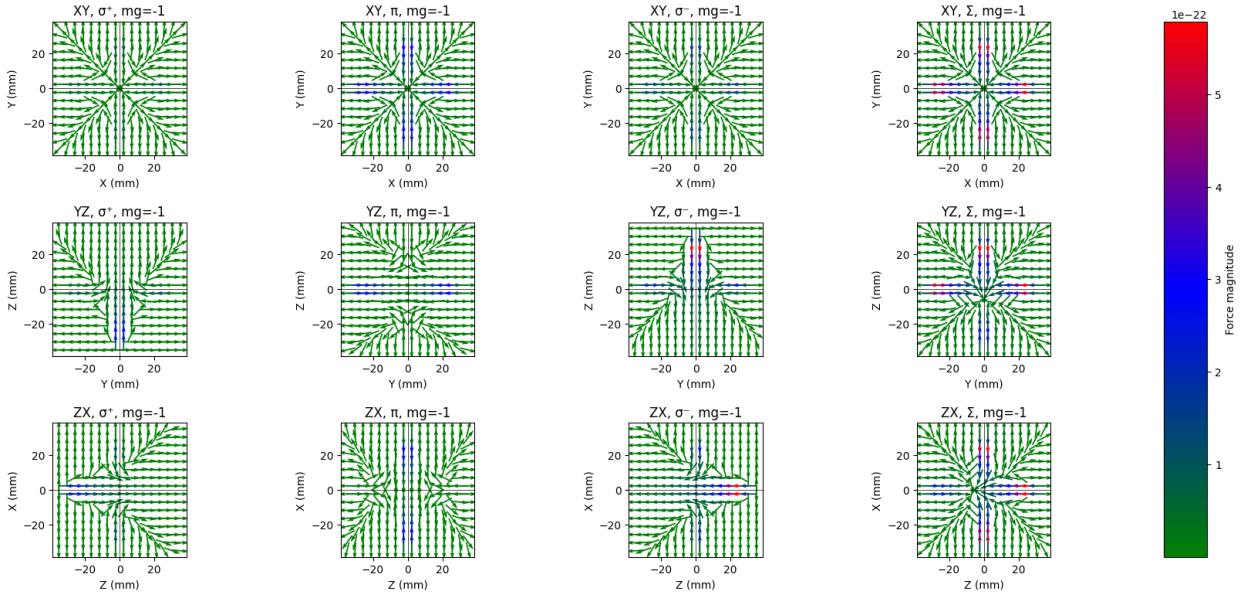

FIGURE 15. Force field when $m_g = -1$ for a stationary atom.

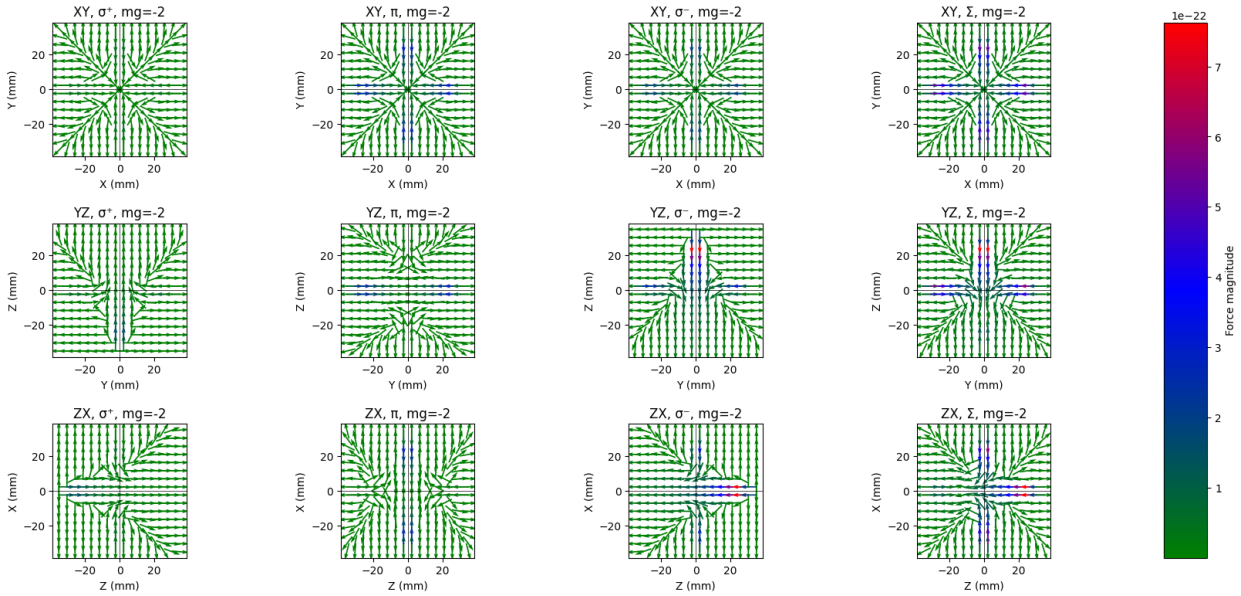

FIGURE 16. Force field when $m_g = -2$ for a stationary atom.

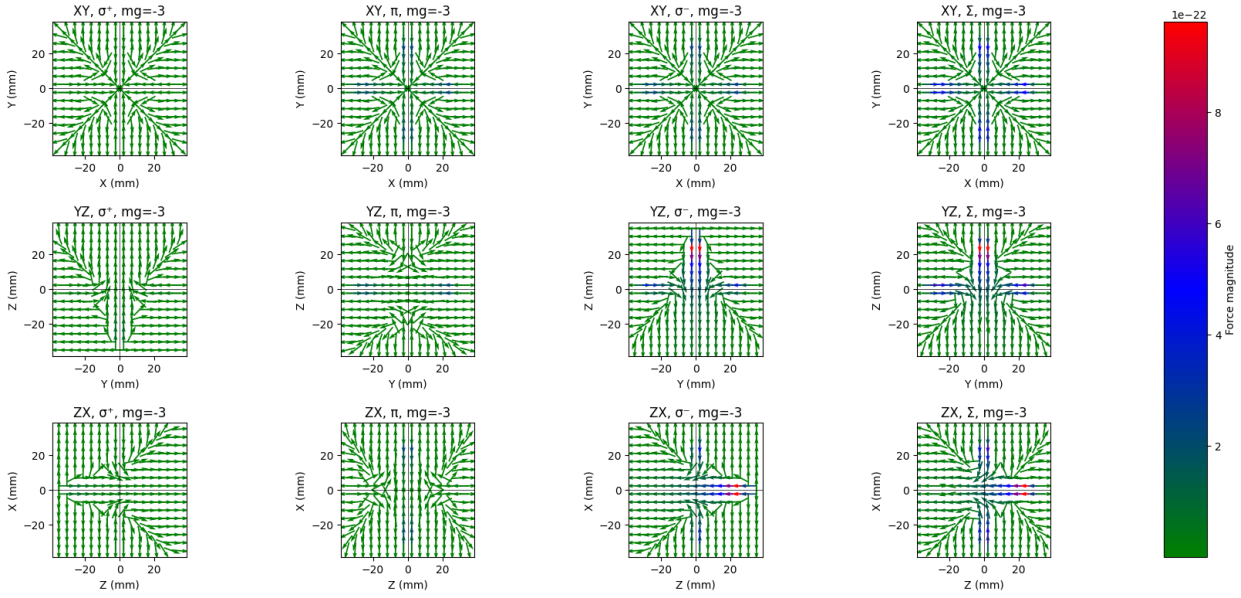

FIGURE 17. Force field when $m_g = -3$ for a stationary atom.

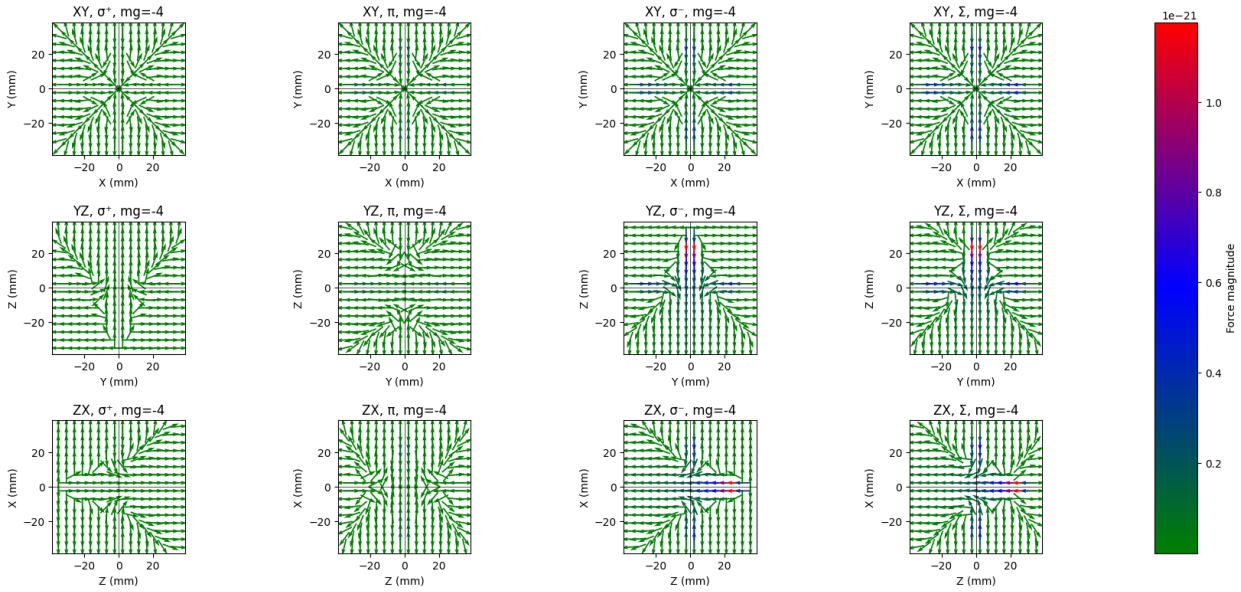

FIGURE 18. Force field when $m_g = -4$ for a stationary atom.

Appendix C: Force Field for Various Divergent Angles

Shown below are the simulated force fields for each ground state, calculated under the conditions described in the Monte Carlo Simulation Algorithm section, with a beam ellipticity of 45° at the ground state of $m_g = 0$.

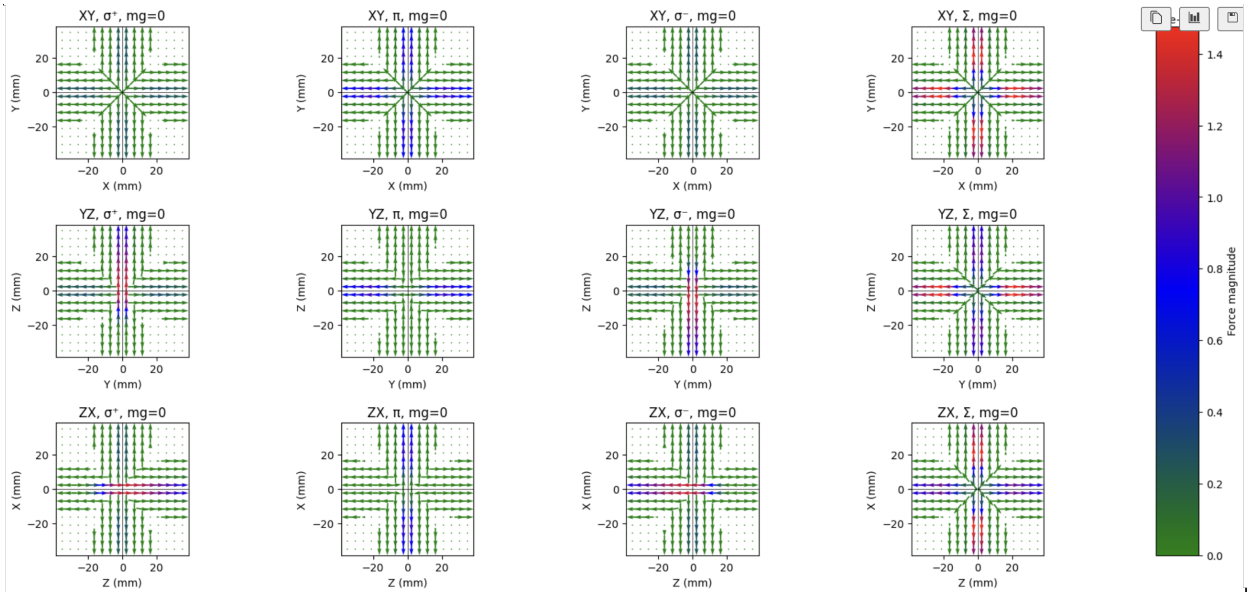

FIGURE 19. Force field when the divergent angle is 5°.

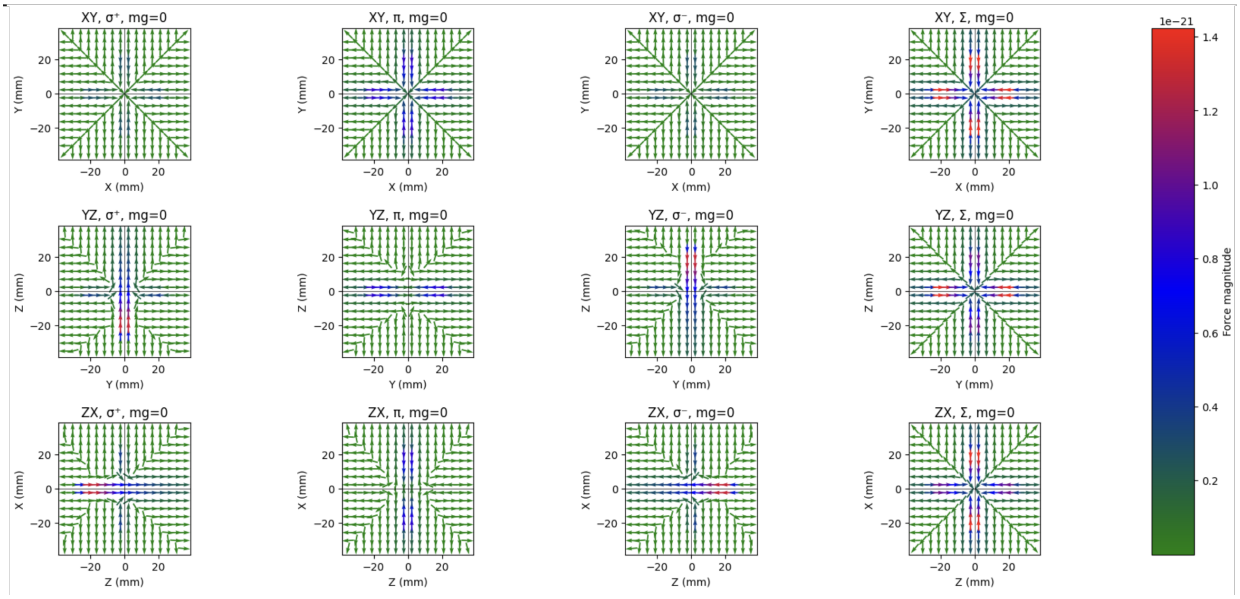

FIGURE 20. Force field when the divergent angle is 12°.

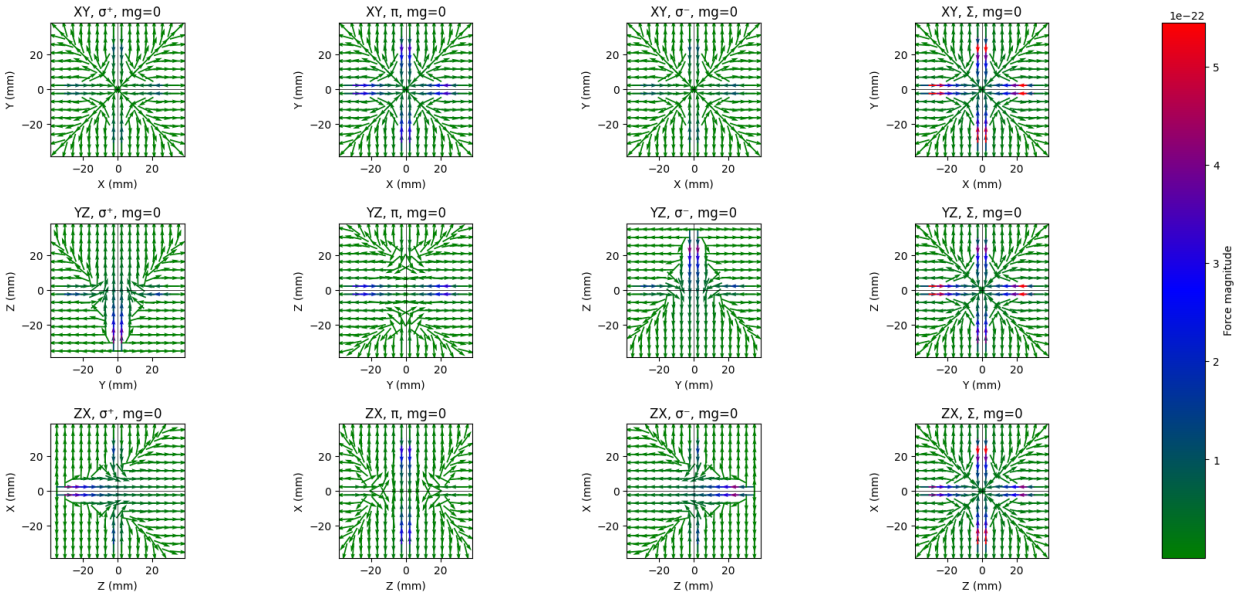

FIGURE 21. Force field when the divergent angle is 22°.

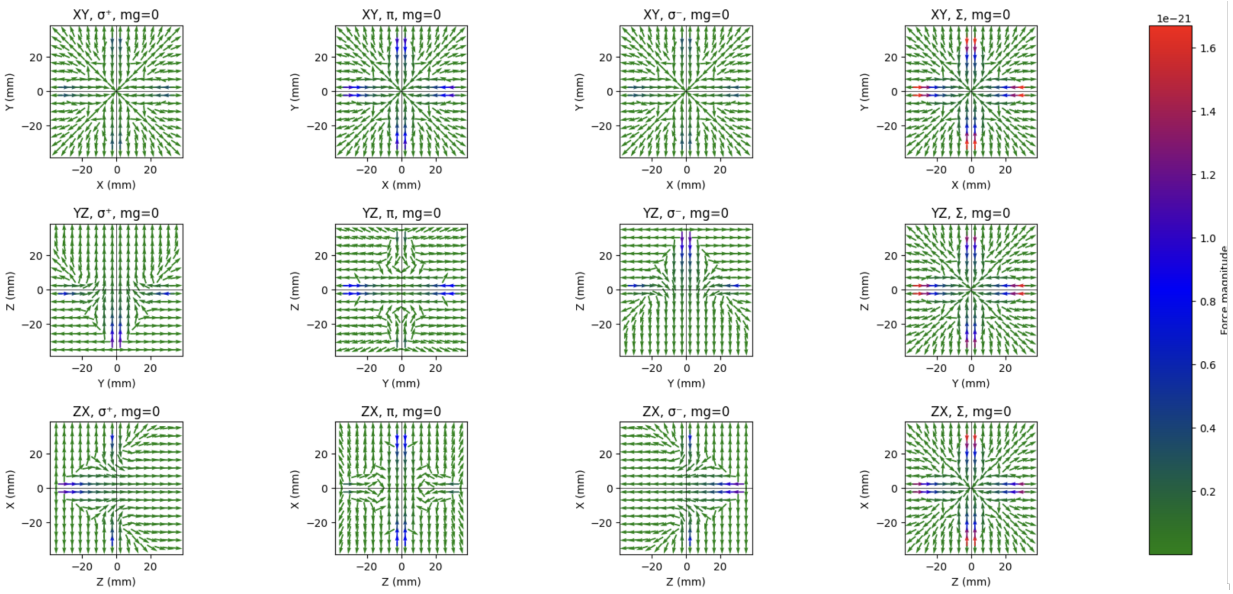

FIGURE 22. Force field when the divergent angle is 35°.

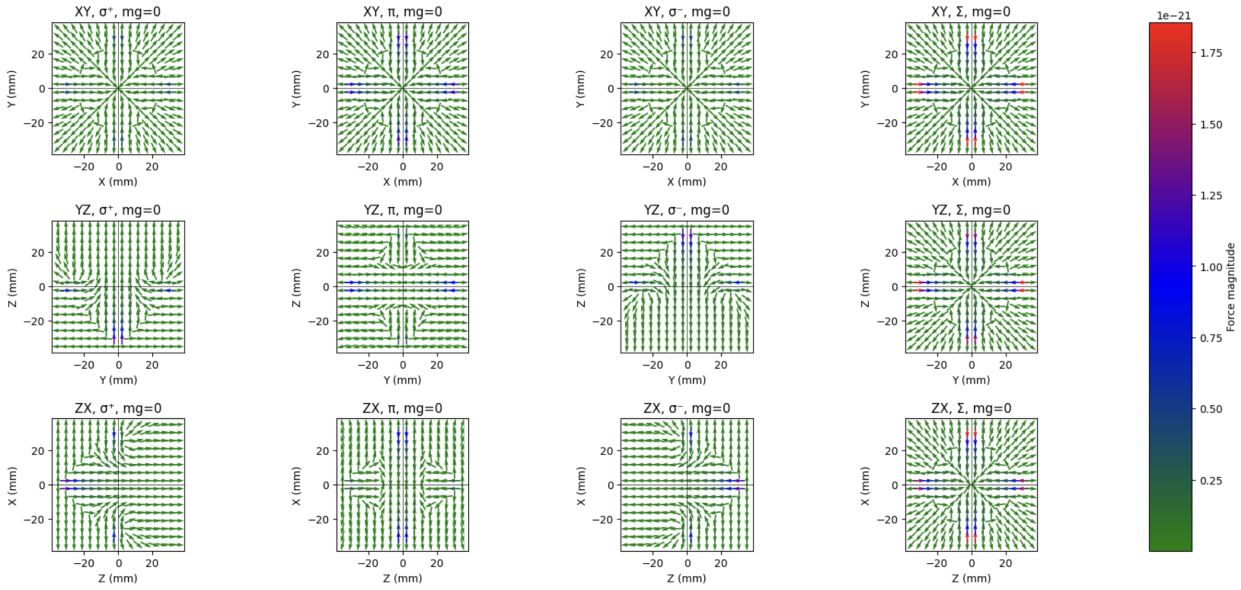

FIGURE 23. Force field when the divergent angle is 45°.

Appendix D: Force Field for Various Elliptical Angles

Shown below are the simulated force fields for each ground state, calculated under the conditions described in the Monte Carlo Simulation Algorithm section, with a beam divergence of 22° at the ground state of $m_g = 0$.

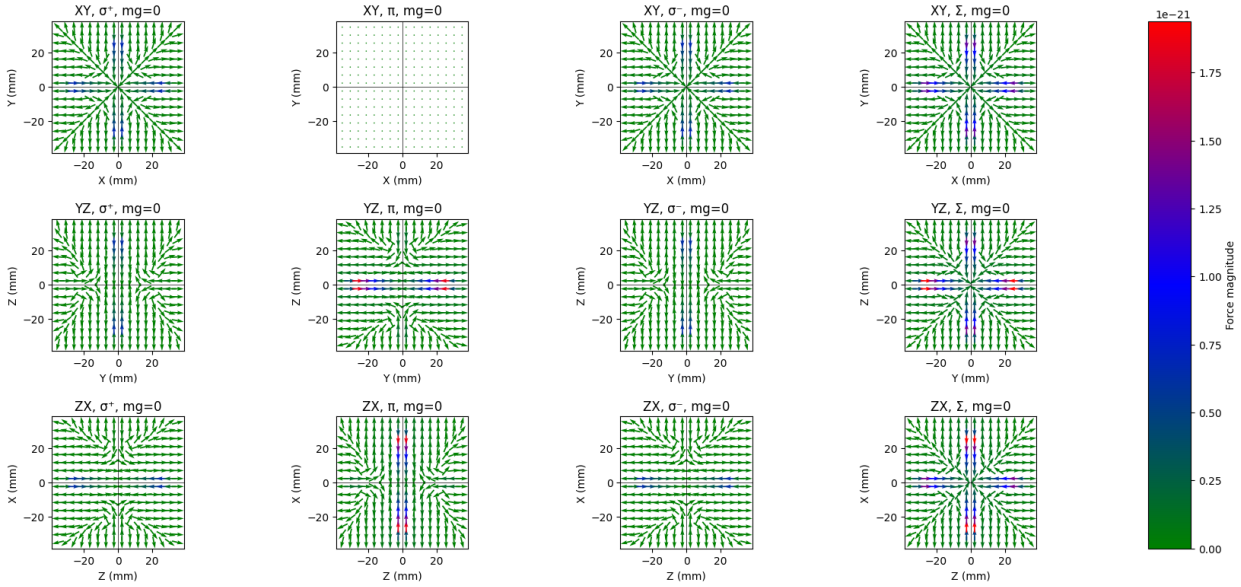

FIGURE 24. Force field when the elliptical angle is 0°.

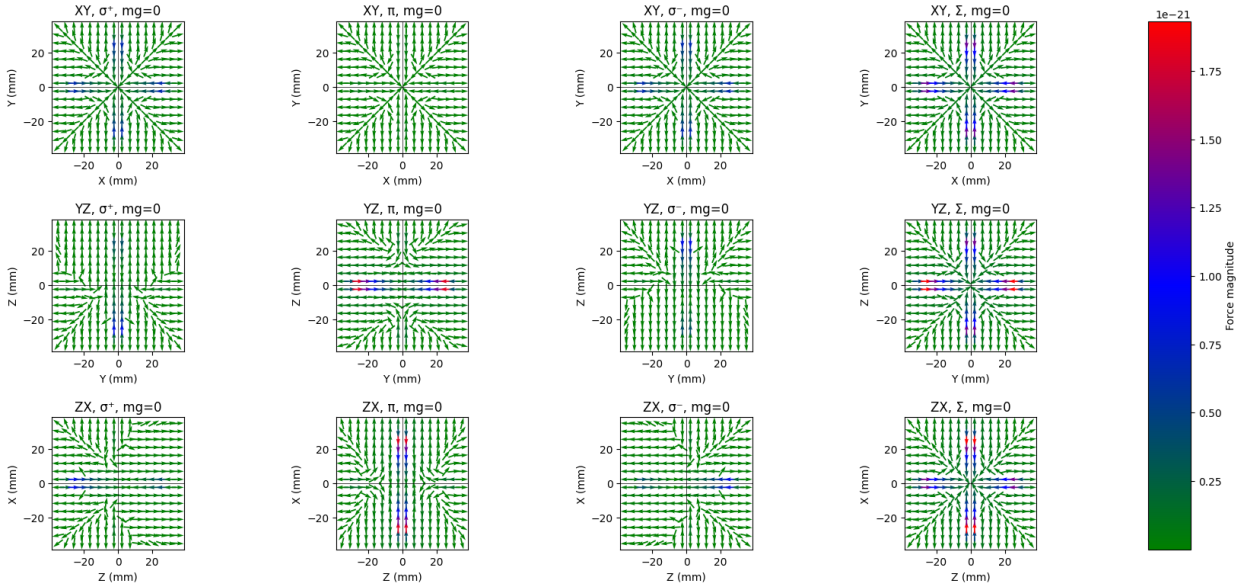

FIGURE 25. Force field when the elliptical angle is 10°.

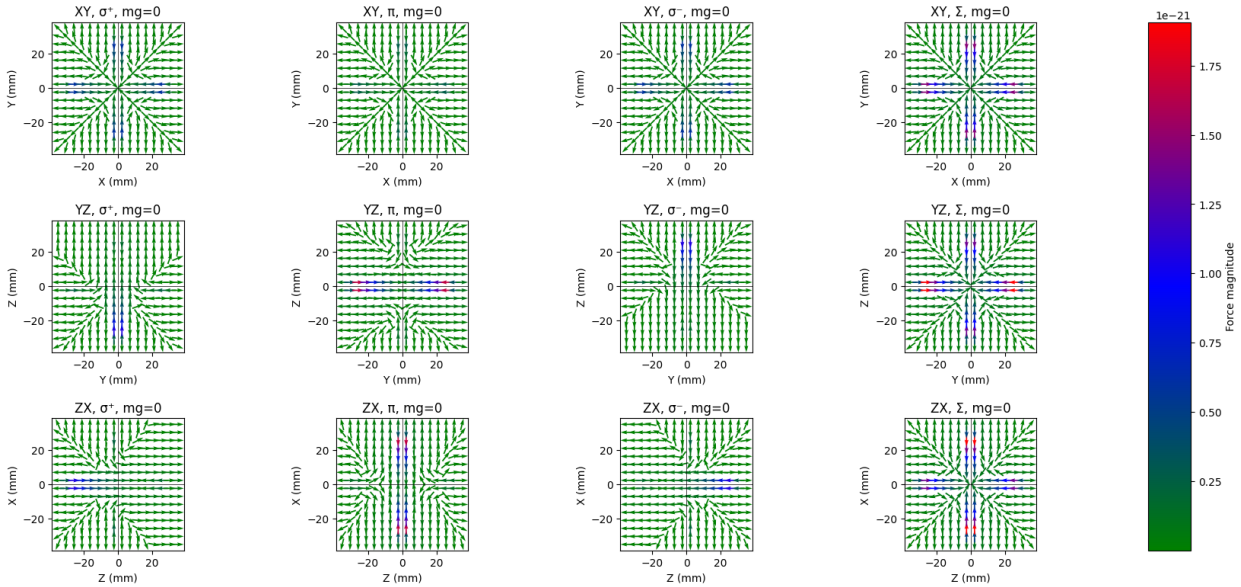

FIGURE 26. Force field when the elliptical angle is 20°.

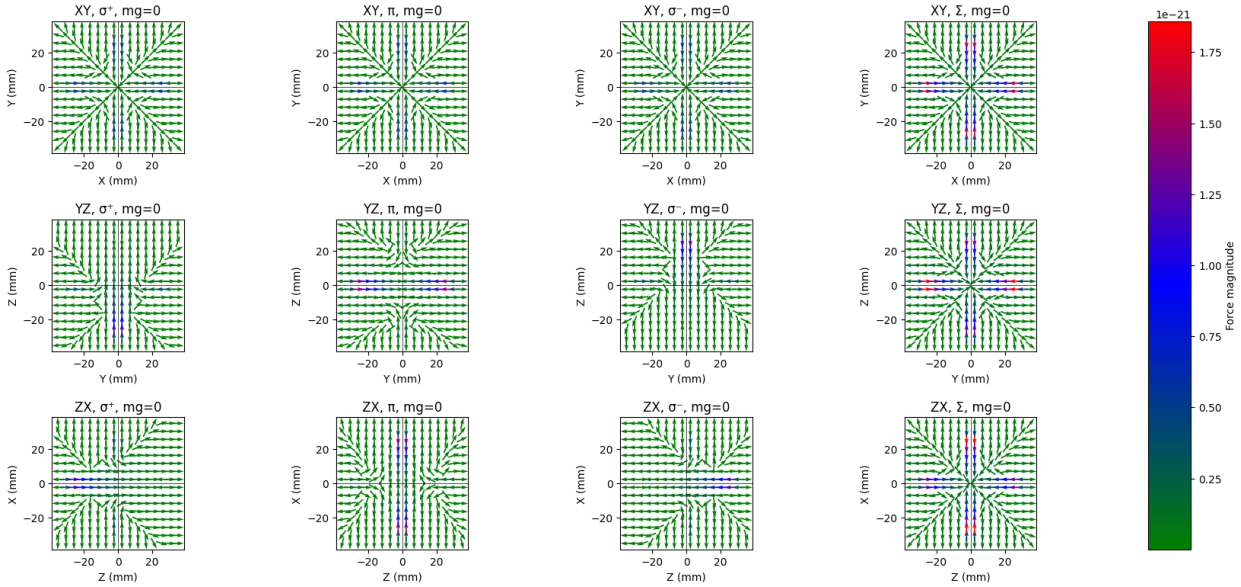

FIGURE 27. Force field when the elliptical angle is 30°.

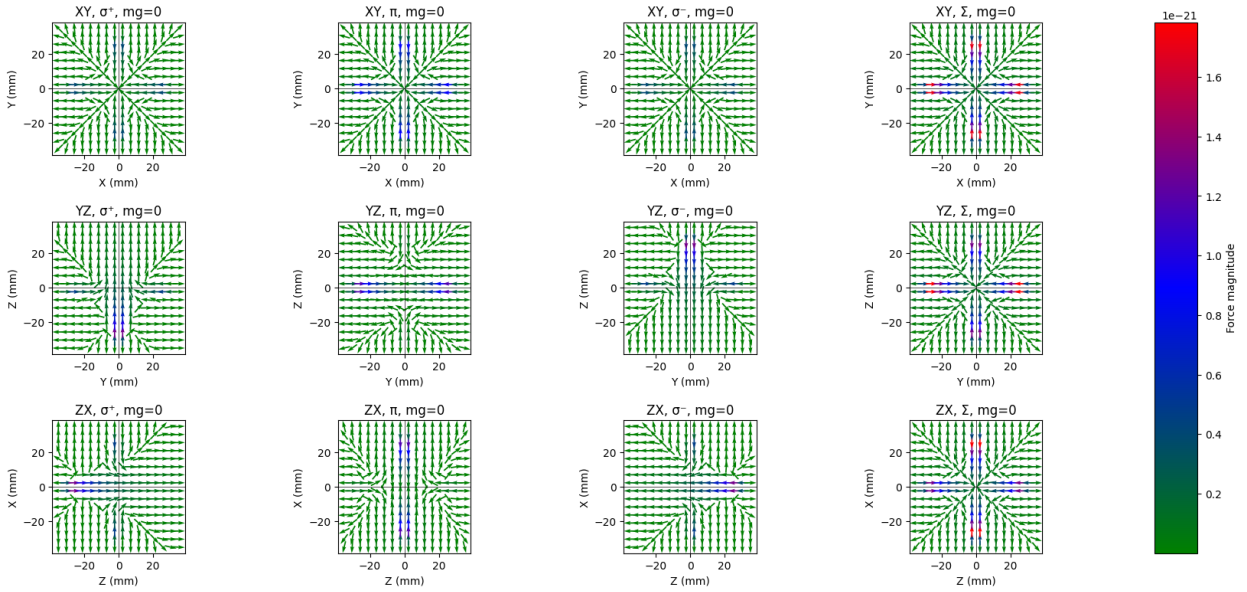

FIGURE 28. Force field when the elliptical angle is 40°.

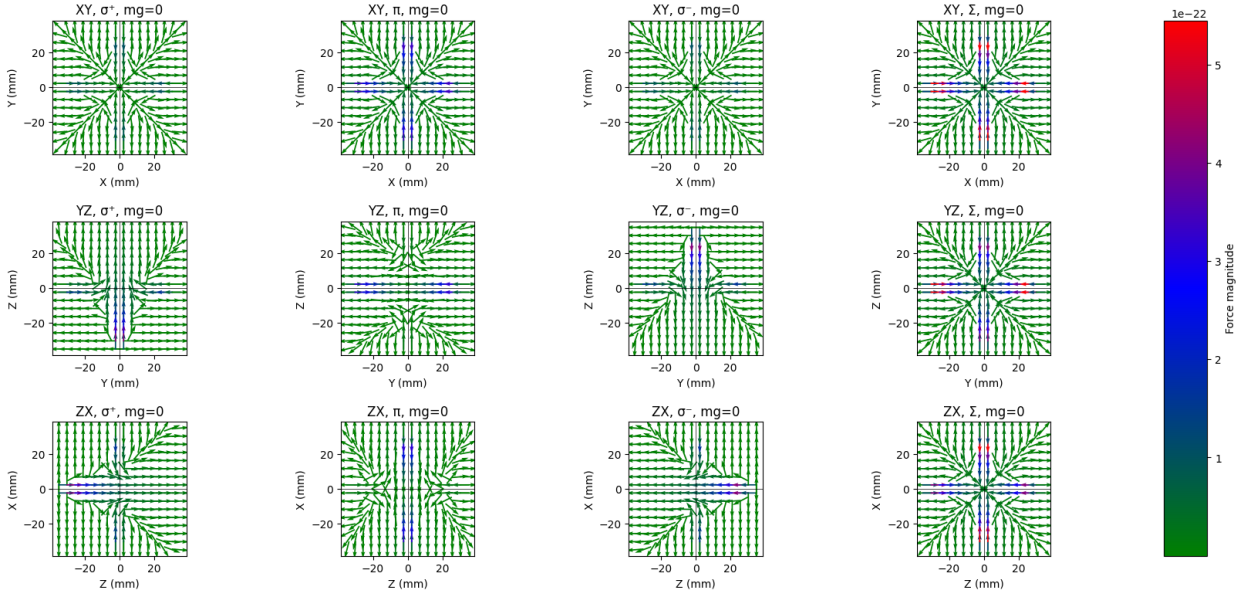

FIGURE 29. Force field when the elliptical angle is 45°.

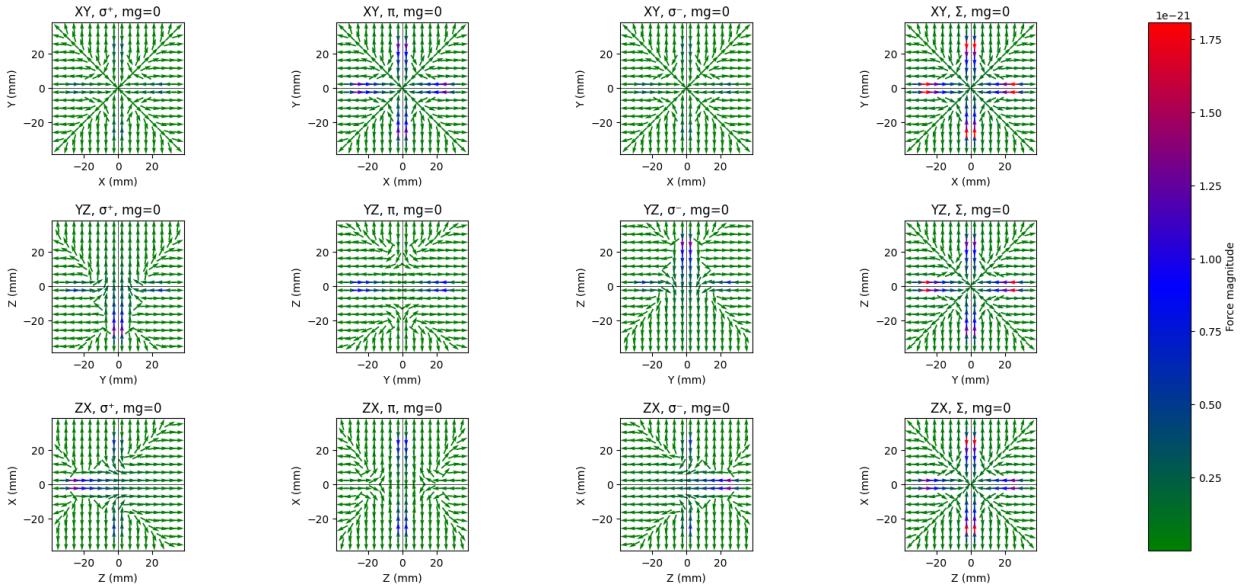

FIGURE 30. Force field when the elliptical angle is 50°.

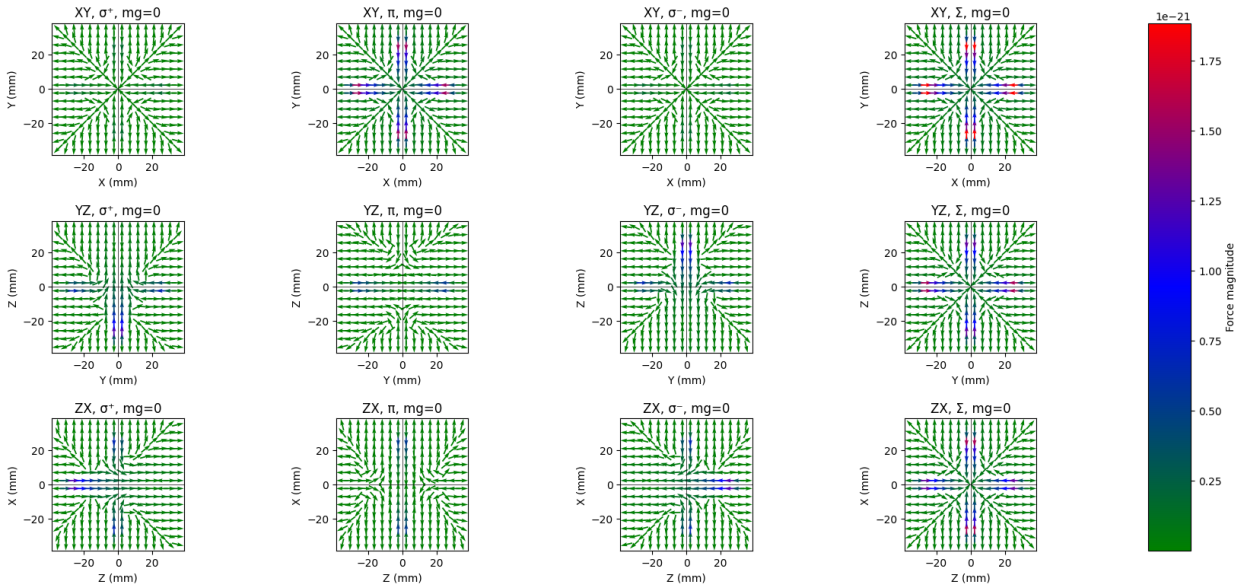

FIGURE 31. Force field when the elliptical angle is 60°.

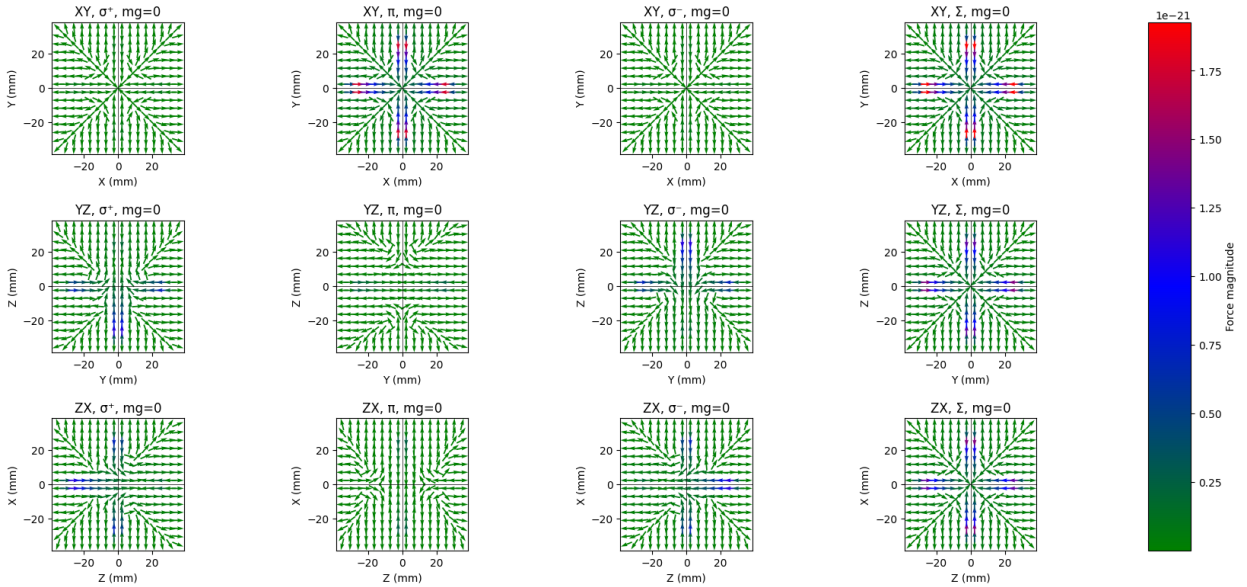

FIGURE 32. Force field when the elliptical angle is 70°.

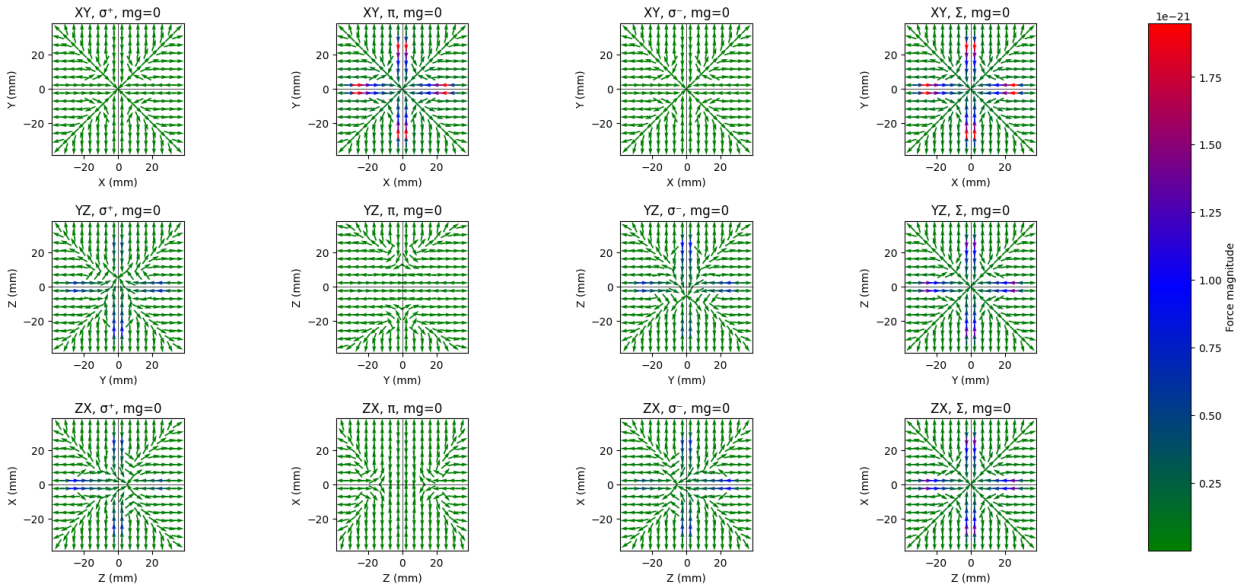

FIGURE 33. Force field when the elliptical angle is 80°.

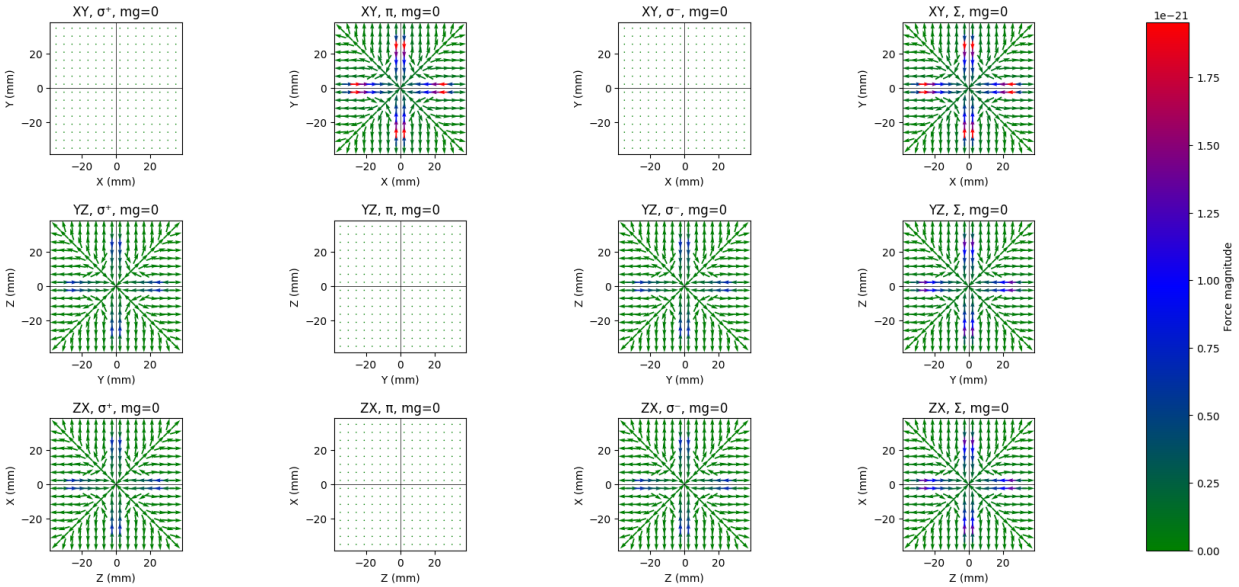

FIGURE 34. Force field when the elliptical angle is 90°.

Appendix E: Detailed Monte Carlo Simulation Algorithm

Let the atom be on a ground-state Zeeman sublevel characterized by m_g. The excited state magnetic quantum number after absorption depends on the polarization of the absorbed photon:

$$\Delta m_{\text{abs}} = \begin{cases} +1, & \text{for } \sigma^+, \\ 0, & \text{for } \pi, \\ -1, & \text{for } \sigma^-, \end{cases} \tag{13a}$$

$$m_e = m_g + \Delta m_{\text{abs}}. \tag{13b}$$

The effective detuning seen by the beam j includes the Doppler shift,

$$\Delta_{\text{eff},j} = \delta_0 - k_0 \hat{k}_j \cdot \mathbf{v}, \tag{14a}$$

where $\mathbf{v}$ is the atomic velocity and δ_0 is the red-detuning from resonance.

The transition strength of each spherical component is weighted by the relevant squared Clebsch–Gordan factor $C_q^2(m_g \to m_e)$. Then, the squared Rabi frequency contribution from beam j polarization q is

$$\Omega_{jq}^2 = \frac{\Gamma^2}{2} \frac{I_{qj}}{I_{\text{sat}}} C_q^2(m_g \to m_e)[3]. \tag{15a}$$

For standard TROOP, the intensities of each polarity are dependent on the position of the atom. For a quantization axis along $\hat{z}$, an atom displaced by z from the origin with beam focus distance a shows an approximately linear dependence of $I(\sigma^{\pm})$ on z. With the quantization axis along $\hat{x}$ or $\hat{y}$, a displacement ξ along that axis yields the analogous linear relations [1],

$$I(\sigma_+) = \left(1 - \tfrac{2z}{a}\right) I(\pi), \tag{16a}$$

$$I(\sigma_-) = \left(1 + \tfrac{2z}{a}\right) I(\pi), \tag{16b}$$

$$I(\sigma_+) = \left(1 + \tfrac{\xi}{a}\right) I(\pi), \tag{16c}$$

$$I(\sigma_-) = \left(1 - \tfrac{\xi}{a}\right) I(\pi). \tag{16d}$$

Subsequently, the scattering rate for that beam is

$$R_{jq} = \Gamma \frac{\frac{\Omega_{jq}^2}{2}}{\Delta_{\text{eff},j}^2 + \frac{\Omega_{jq}^2}{2} + \frac{\Gamma^2}{4}}. \tag{17a}$$

The scattering rate for that channel is

$$R_{jq} = \Gamma \frac{\frac{\Omega_{jq}^2}{2}}{\Delta_{\text{eff},j}^2 + \frac{\Omega_{jq}^2}{2} + \frac{\Gamma^2}{4}}. \tag{18a}$$

Positive rates are collected in all combinations (j,q) to form the total scattering rate $R_{\text{tot}} = \sum_{j,q} R_{jq}$ [4]. In a small time step Δt, let the probability that a scattering event occurs be $P = R_{\text{tot}} \Delta t$, such that $P \ll 1$. A Monte Carlo scattering event occurs when a uniformly distributed random number between 0 and 1, $U[0,1]$, is smaller than P [5].

Once the scattering event is determined, beam selection is performed by computing the normalized probabilities

$$p_j = \frac{R_j}{R_{\text{tot}}} \tag{19a}$$

for each possible polarization j. Then, a random channel index i is drawn from this discrete distribution.

Thus, the momentum change of the atom is

$$\Delta\vec{v} = \frac{\hbar k_0}{m}\left(\hat{d} + \hat{k}_{\text{em}}\right)[5], \tag{20a}$$

where $\hat{d}$ is the photon direction

$$\vec{d} = \vec{r} - \vec{r}_{\text{beam},i}, \quad \hat{d} = \frac{\vec{d}}{\|\vec{d}\|} \tag{21a}$$

and $\hat{k}$ is a random recoil kick

$$\hat{k}_{\text{em}} = (\sin\theta\cos\phi,\ \sin\theta\sin\phi,\ \cos\theta), \tag{22a}$$

where $\phi = 2\pi \cdot U[0,1]$, $\cos\theta = 2 \cdot U[0,1] - 1$, and $\sin\theta = \sqrt{1-\cos^2\theta}$, where $U[0,1]$ is an uniform random number on the interval [0,1]. If the scattering event does not happen, the atom propagates ballistically.